FAR INFRARED SPECTROSCOPY AND IMAGING OF Cu(In, Ga)Se$_2$ LAYERS

L. Minkevičius [a], S. Balakauskas [a], M. Šoliūnas [a], R. Suzanovičienė [a], J. Uzėla [a], G. Molis [b],

R. Juškėnas [a], A. Selskis [a], G. Niaura [a], G. Valušis [a,c], and V. Tamošiūnas [a,c]

[a] *Center for Physical Sciences and Technology, Savanorių 231, LT-02300 Vilnius, Lithuania*
E-mail: linas.minkevicius@ftmc.lt
[b] *TeraVil Ltd, A. Goštauto 11, LT-01108 Vilnius, Lithuania*
[c] *Faculty of Physics, Vilnius University, Saulėtekio 9-III, LT-10222 Vilnius, Lithuania*

The Fourier transform infrared spectroscopy (FT-IR), terahertz time domain spectroscopy (THz-TDS), and terahertz imaging were applied to study the properties of Cu(In, Ga)Se$_2$ (CIGS) layers grown on Mo/soda lime glass substrate. Correlation between the Infrared reflectivity spectrum around 5–7 THz (167–233 cm^{-1}), Raman spectra, and X-ray diffraction data is investigated for samples grown on the molybdenum layer of approximately 1 μm in thickness. Also, transparency of CIGS layers was demonstrated for frequencies down to several hundred gigahertzes. Such transparency opens possibilities for future three-dimensional characterization of CIGS structures using phase sensitive imaging.

Keywords: solar cells, chalcogenide solar cells, terahertz time domain spectroscopy, FT-IR spectroscopy

PACS: 88.40.H-, 88.40.jn, 78.47.D-

1. Introduction

The efficiency of Cu(In,Ga)Se$_2$ (CIGS) solar cells recently reached the 20.3% record [1] for small solar cells and 15.5% for large area flexible modules [2]. Such numbers mean that CIGS technology is already a viable alternative to silicon solar cell based modules and is expected by industry experts to be one of the most promising technologies for cost reduction of photovoltaics [3]. However, one of the remaining challenges for large scale CIGS solar cell production is the remaining lack of diagnostics tools that could respond to rapid processing and feedback for adjusting real-time processes [4].

The purpose of this paper is to investigate the properties of CIGS layers from the mid-IR range down to sub-THz frequencies and to evaluate the possibilities to use compact imaging systems [5] of these ranges as diagnostics tools for CIGS production: monitoring of thickness, crystal formation results, or detection of metal contact faults.

2. Experiment

A single quaternary chalcogenide CIGS target (pioneer materials, diameter 20 cm, thickness 6.35 mm, composition: Cu 22.8 at %, In 20 at %, Ga 7 at %, Se 50.2 at %) and the Alcatel SCM 650 RF magnetron sputtering equipment were employed to deposit several Cu(In,Ga)Se$_2$ samples with parameters listed in Table 1. For sample CIGS-12, an additional layer of approx. 50 nm thick Cu was deposited from the separate Cu target of the same size in the same equipment.

Table 1. Deposition parameters.

Sample	Substrate	Power, W	Target distance (mm)	CIGS thickness (μm)	Anealing temperature T, °C	Duration, min
CIGS-9	Glass	500	60	1.4	524	15
CIGS-12	Glass + Mo	500	60	1.3+0.05 Cu	523	5
CIGS-19	Glass + Mo	400	90	1.5	530	40
CIGS-20	Glass + Mo	300	60	1.5	530	40

During deposition, selenium vapour was introduced from Se pellets on the Cu sheet, covering a negligible area of the target.

The Nicolet 8700 FT-IR spectrometer equipped with 30° specular reflectance accessory was used to record spectra in near-IR (350–7400 cm⁻¹) and far-IR (50–600 cm⁻¹) ranges. A KBr beam splitter and DTGS TEC detector combination was used for mid-IR measurements, and a combination of a solid substrate beam splitter and DTGS detector with a polyethylene window for far-IR measurements. The Peak Scientific PG28L air purifier was used to partially remove H_2O and CO_2 absorption lines. An aluminum coated mirror served as a reference for reflection coefficient measurement.

A phase composition of the deposits was examined by an X-ray diffractometer D8 Advance (*Bruker AXS*) with Cu K$_\alpha$ radiation ($\lambda = 1.54183$ Å, $U_a = 40$ kV, $I_a = 40$ mA) separated by a curved multilayer monochromator mounted on the primary beam. Symmetrical $\Theta/2\Theta$ geometry and grazing incidence (GIXRD) techniques were used, and in the latter case the incidence angle (Θ angle) was 0.5°. The XRD patterns were measured in 2Θ range from 10 to 60° in a step scan mode: step size ($\Delta2\Theta$) 0.04°, counting duration 5 s.

A T-spec terahertz time-domain spectrometer (THz-TDS) (*TeraVil-Ekspla*) with the imaging function was employed to record spectra and THz images below 3 THz, where usability of the Nicolet 8700 FT-IR spectrometer was limited by the signal to noise ratio of available source and detector. The photoconductor antenna illuminated by ultra-short laser pulses was used for THz radiation and detection. Second harmonic radiation from a femtosecond fibre laser (*Toptica Photonics*) was used as a source of 90 fs duration pulses of 790 nm wavelength. The pumping beam was divided into two beams. By scanning the fast optical delay line in 10 Hz frequency, the waveform of an electrical field of THz radiation was build. The Fourier transform of the waveform gives the spectral content of THz radiation and phase information. Each scanned curve was averaged 16 times, the pixel size was 500×500 μm², and the images consisted of up to 50×50 pixels.

To confirm the crystalline structure of one of the samples, Raman measurements were performed with 632.8 nm excitation by using the Raman microscope inVia (*Renishaw*) equipped with a grating containing 1800 grooves/mm. Laser power at the sample was 1 mW. Raman spectra were taken using a 50×/0.75 NA objective lens. Integration time was 100 s. Parameters of the peaks were determined by fitting the experimental contour by Gausian-Lorentzian form components using Grams386 software.

3. Results

The reflectance spectra of samples CIGS-9 and CIGS-12 and of the open glass surface of CIGS-9 substrate are presented in Fig. 1 As one can clearly see, a regular Fabry-Perot interference pattern appears in the near-IR range for sample CIGS-9. This pattern is expected for a thin semiconductor layer due to interference effects in case of a low loss in this layer. The XRD pattern presented in Fig. 2 confirms that the CIGS layer indeed was grown in case of this sample. In the near-IR range, glass is transparent; therefore, only a small difference of interference fringes is observed depending on the side of the CIGS-9 sample. Spectral features in far-IR and mid-IR ranges are more complex. However, most are quite easy to explain if we consider the properties of the substrate (in this case, glass). Its measured reflectance spectrum for longer wavelengths essentially repeats the one well know from the THz reflectance database [6]. Glass is an effective absorber from the far-IR range to the wavelengths of several microns (or approx. 4000 cm⁻¹), and what we see in Fig. 1 in case of CIGS-9 is its reflectance spectrum influenced by the thin layer of the semiconductor
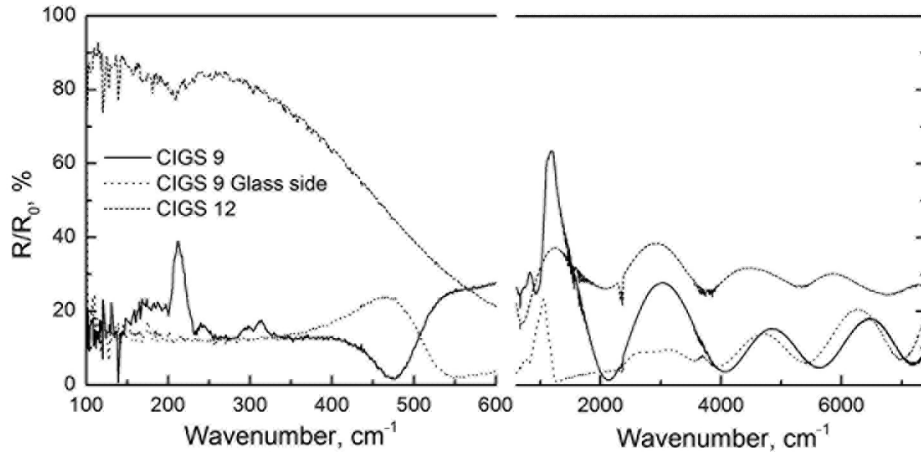
Fig. 1. Reflectance spectra of samples CIGS-9 and CIGS-12 in 100–600 cm^{-1} (left) and 600–7400 cm^{-1} (right) ranges. Reflectance of glass substrate side was also recorded for sample CIGS-9 (indicated by "Glass side"). Unreliable data points corresponding to strongest atmospheric absorption lines are removed from far-IR reflectance spectra. The same procedure was also applied to all far-IR spectra presented later in this paper.

on the top of it. There are, however, a couple of exceptions – peaks at approx. 175 and 208 cm^{-1} cannot be attributed to the properties of glass, since its spectrum is very broad in this part.

The situation is different for sample CIGS-12. Here, the thick molybdenum contact acts as a nearly perfect mirror for the lowest frequency waves, leading to reflection coefficients in excess of 80% in
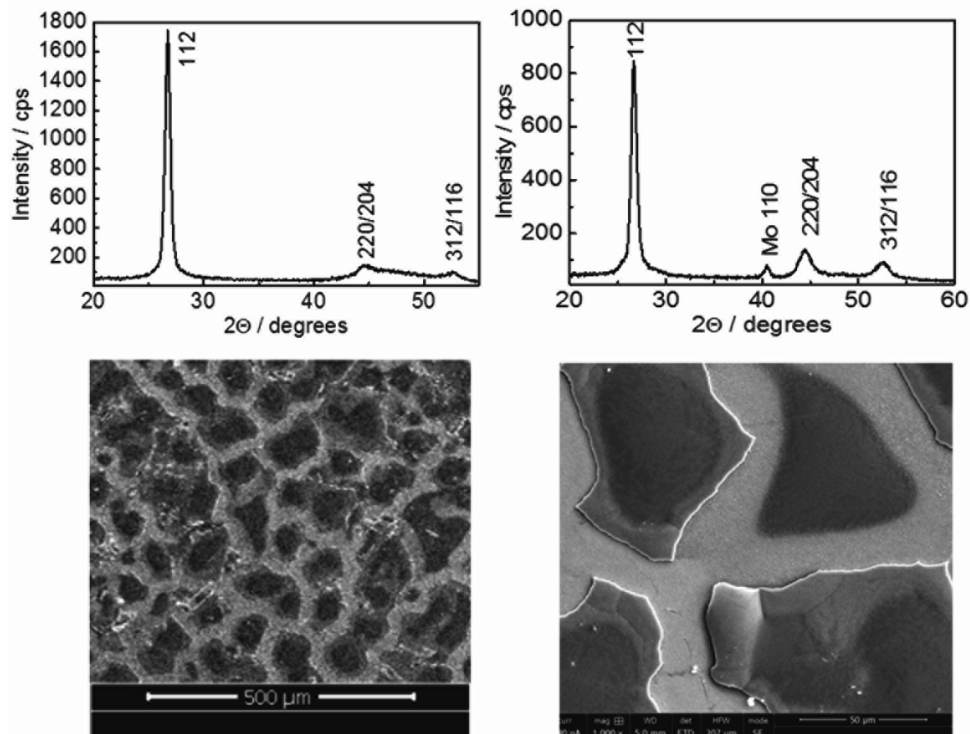

Fig. 2. XRD patterns of samples CIGS-9 (top left) and CIGS-12 (top right) and SEM images of sample CIGS-12, scale 500 μm (bottom left) and scale 50 μm (bottom right).

the far-IR range. In addition, differently from the previous case, reflectivity exceeds 20% at the minimum in the near-IR range, and the modulation depth of the spectrum is much lower. SEM images (Fig. 2) reveal a possible cause of these spectral features – this particular sample is actually composed of multiple "islands" of various sizes of the order of tens of microns. A SEM image at higher 1000× magnification (Fig. 2, bottom right) confirms that "islands" are areas with an additional highly non-uniform layer. This means that in the case of FTIR measurements reflectance is influenced both by averaging reflectance from two types of surfaces and by scattering.

This averaging is not present in case of two other samples, CIGS-19 and CIGS-20, presented in Fig. 3. Here, large area microcrystalline layers were successfully fabricated with fairly uniform coverage within up to tens of square centimetres. Also, sample CIGS-20 had a fairly large (centimetres long and several millimetres wide) area where

the CIGS layer peeled off during growth and the thinner layer formed on the top of molybdenum (area "E"), while bottom metallization defect was created in case of sample CIGS-19 by covering the substrate with a metal wire. This area is indicated as "loop" in Fig. 3.

The reflectance spectra of samples CIGS-19 and CIGS-20 are presented in Fig. 4, while SEM images and XRD patters of several areas are collected in Fig. 5. Slightly different growth conditions or condition of the target led to substantial differences in the size of crystallites and surface roughness as XRD patterns and SEM images of Fig. 5 witness. The mid-IR spectra of sample CIGS-20 (Fig. 4) are typical examples of the illustration of the interference in a thin layer. Such measurement can be used immediately to compare the thickness in a contactless way. The estimation of the refractive index based on fringe spacing and Table 1 data leads to the values in the range of $n = 2.3$–2.4, which is lower than the recently measured values of 2.5–3 [7],
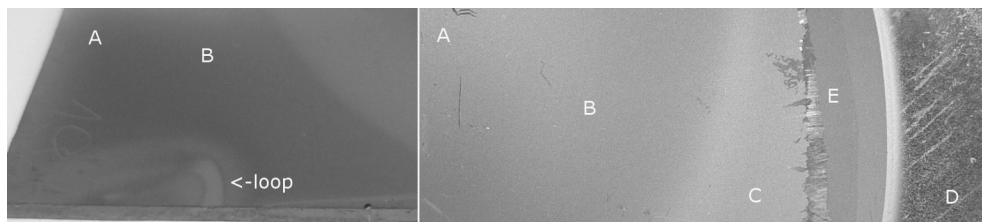

Fig. 3. Optical photographs of samples CIGS-19 (left) and CIGS-20 (right). Letters indicate approximate positions used for further measurements. Sample CIGS-20 had a fairly large area ("E"), where the CIGS layer pealed off during growth and the thinner layer formed on the top of molybdenum. In case of sample CIGS-19, "loop" indicates the area, where substrate was covered during Mo contact growth to form a metallization defect below the CIGS layer.
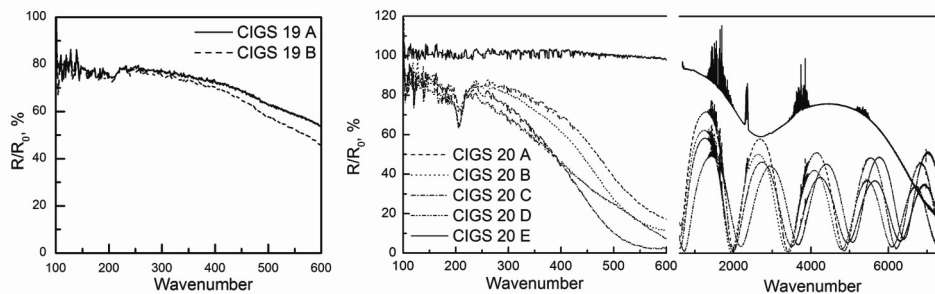

Fig. 4. Reflectance spectra of 100–600 cm^{-1} (CIGS-19 on the right, CIGS-20 in the centre) and 600–7400 cm^{-1} (CIGS-20, right panel). Letters after sample numbers indicate the positions as presented in Fig. 3.
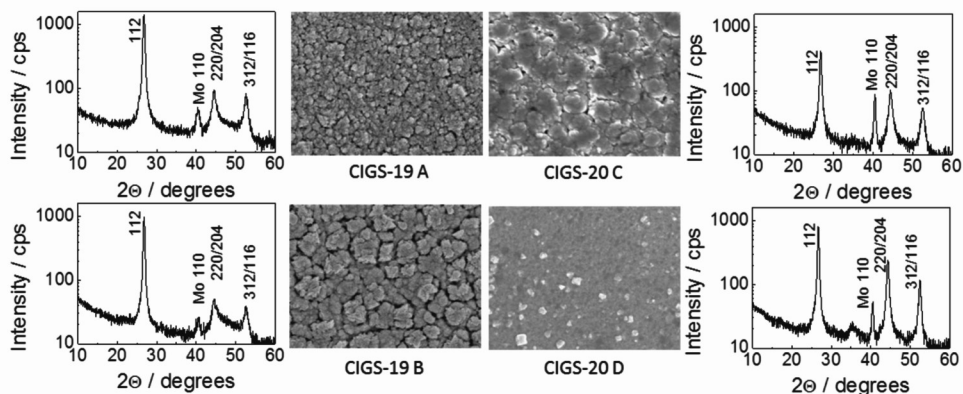
Fig. 5. XRD patterns and SEM images of 4×3 μm areas of samples CIGS-19 and CIGS-20.

but this probably can be attributed to a reduction of layer thickness during recrystallization or thickness variations across the sample. Interference fringes from the thinner CIGS layer (area "E" indicates that an approximately four times thinner layer was grown here after the original one was lost during the growth. Another interesting feature once again occurs at above 200 cm^{-1} – here, a sharp negative peak is observed for sample CIGS-20. The reverse of direction in comparison with CIGS-9 would be natural if we assume that these features are caused by the strong absorption in the layer, which eliminates the reflections from the substrate for this frequency. In this case, the reflection coefficient would be mostly influenced by the properties of the material and, therefore, it has a similar value both for CIGS-20 and CIGS-9 – approx. 60%. In the case of CIGS-19, only minor changes in reflectivity of around 200 cm^{-1} occur here. This probably could be attributed to the poorer quality of the crystalline material, which was evidenced by XRD patterns and SEM images presented in Fig. 5.

Raman spectroscopy was employed to reveal the properties of investigated layers in more detail. Figure 6 compares the normalized Raman spectra of four studied samples. The most intense band at 177–180 cm^{-1} belongs to A$_1$ mode of CIGS [8]. This mode can be described as vibration of Se anions in the *x-y* plane. The frequency of this mode increases linearly with increasing Ga content [8, 9]. The low intensity shoulder at 247 cm^{-1} probably belongs to Cu$_{2-x}$Se domains [8]. The shoulder near 162 cm^{-1} indicates the presence of molecularity [Cu]/[In+Ga] lower than 1 [10], which was expected in case of our target compo-

sition. CIGS-20D does not show any sign of 162 cm^{-1} peak (Fig.6(d)). It should also be noted that sample CIGS-20D shows the narrowest A$_1$ peak at 177 cm^{-1}, indicating the highest crystalline quality for this film compared with other studied samples [11].
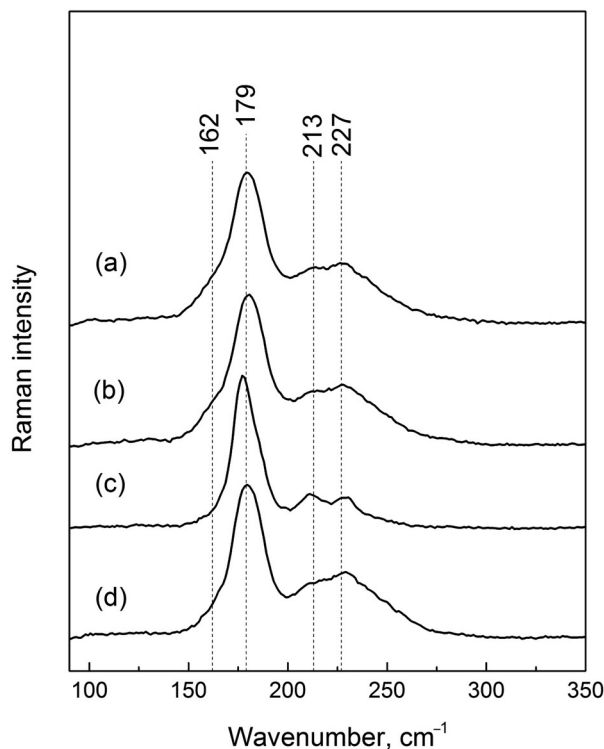

Fig. 6. Raman spectrum of CIGS film in 80–350 cm^{-1} spectral region. Excitation wavelength is 632.8 nm (0.5 mW). Samples: (a) CIGS-19B, (b) CIGS-19A, (c) CIGS-20D, (d) CIGS-20C. Spectra are normalized to the intensity of the most intense peak near 179 cm^{-1}. Spectra are shifted vertically for clarity.

Several key features should be mentioned when comparing all presented FTIR and Raman data. First, despite the tallest peak in Raman spectra at approximately 179 cm^{-1}, spectral features are barely visible in far-IR reflectance spectra. The most pronounced spectral feature (increase of reflectivity in case of glass substrates and decrease in case of Mo covered substrate) appears at approx. 208–210 cm^{-1}. These values are close to the ones expected for B_2 or E modes [12]; however, the presence of atmospheric absorption in our current FTIR setup prevents a more precise evaluation if the position of this feature matches the 213 cm^{-1} line in Raman spectra.

The composition of sample CIGS-19 in 3 locations and of sample CIGS-20 in 5 locations was investigated in more detail using the SEM-EDS equipment in order to reveal a possible cause for the observed differences in surface smoothness. Results are summarized in Table 2. As one can clearly see, sample CIGS-19 is average deficient in copper while sample CIGS-20 is copper rich. Cu excess at the starting stages of CIGS growth is a known recipe for smoother CIGS layers and larger grains employed in case of devices with record efficiency (such as [1]); therefore, it could also contribute to smoother layers in our case.

The combination of strong atmospheric absorption, low power of the source, and low sensitivity of FTIR detectors substantially restrict measurements at 100 cm^{-1} or below; therefore, the THz-TDS system by *Ekspla-TeraVil* was employed for spectroscopic imaging measurements in the THz range. The results of these measurements are presented in Fig. 7. As expected, the image at 0.5 THz reveals that sample CIGS-12 acts as a nearly perfect (as good as reference gold coated) mirror due to the conductive molybdenum layer, long wavelength, and low thickness of the CIGS layer. The amplitude reflection coefficient is only marginally larger for the thin CIGS layer on glass in comparison with the glass plate, to which the samples were mounted and which is visible between the samples in the THz image.

1 THz image of sample CIGS-19 reveals similar reflectivity as in case of sample CIGS-12, with one exception – the "loop" shaped area not covered with molybdenum is well displayed in the THz image, but not visible in a photograph due to the thick absorbing CIGS layer on the top. As it was mentioned earlier, this "loop" was intentionally produced during the molybdenum deposition step by installing the wire loop on the top of the glass.

This image illustrates that THz imaging can be successfully applied to study defects of the bottom contact even in case of deposition of CIGS on the top. Of course, this problem can be solved for the transparent glass substrate by imaging the sample in the visible range from the bottom and analysing the shades of grey; however, THz imaging has an

Table 2. Atomic ratios of elements (in atomic %) for samples CIGS-19 and CIGS-20 in several locations.

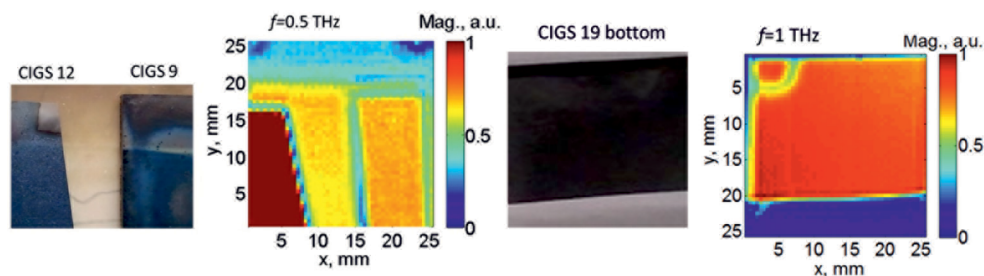| Measurement No.	1	2	3	4	5	Average
Cu/III (CIGS-19)	0.85	0.94	1.05	–	–	0.94
Metals/IV (CIGS-19)	1.11	1.08	1.10	–	–	1.10
Cu/III (CIGS-20)	1.35	1.18	1.28	1.27	1.24	1.26
Metals/IV (CIGS-20)	1.42	1.27	1.14	1.38	1.28	1.29

Fig. 7. Photo and 0.5 THz image of samples CIGS-9 and CIGS-12 (top); photo and 1 THz image of sample CIGS-19 (bottom).

advantage of high contrast without further analysis and would be compatible with opaque dielectric substrates.

4. Discussion

Several key points can be mentioned when summarizing presented results. First, it was demonstrated that spectral features at approx. 177 and 210 cm^{-1}, characteristic of Cu(In, Ga)Se$_2$ lattice vibrations, can be observed directly by far-IR reflectivity measurements even if highly reflective molybdenum substrate is present below the thin semiconductor layer. Therefore, THz imaging in this range would open a possibility of "seeing" CIGS layer formation in production. THz quantum cascade lasers (QCLs) and imaging systems based on them would be ideal for the task in the production environment due to the absence of vibration sensitive parts. Unfortunately, most popular materials for QCLs have strong optical phonon bands in this area, but there is also an ongoing research on this issue [13].

Secondly, interference fringes in the mid-IR range can be applied to study the thickness of the grown layer, and reflectivity modulation depth contains information about the non-uniformity in the CIGS layer. Simple spectroscopic measurement in mid-IR could reveal this information, and solid state replacement for spectrometers in the production environment exists for this task [14].

As our THz imaging results demonstrate, metal contact defects can be revealed at this range even below the CIGS layer, which is absorbing in the visible range. This feature can be potentially applied for inspection of CIGS modules even if semiconductor layers are grown on opaque substrates.

Acknowledgement

References

[1] P. Jackson, D. Hariskos, E. Lotter, S. Paetel, R. Wuerz, R. Menner, W. Wischmann, and M. Powalla, Prog. Photovolt. Res. Appl. **19**, 894 (2011).
[2] http://www.miasole.com/sites/default/files/MiaSole_release_May_24_2012.pdf
[3] http://www.uspvmc.org/roadmap/index.html
[4] R. Noufi and K. Zweibel, Conference Paper NREL/CP-520-39894, in: *Proceedings IEEE 4th World Conference on Photovoltaic Energy Conversion 2006 (WCPEC-4)* (Waikoloa, Hawaii, 7–12 May 2006).
[5] J. Darmo, V. Tamosiunas, G. Fasching, J. Kröll, K. Unterrainer, M. Beck, M. Giovannini, J. Faist, C. Kremser, and P. Debbage, Opt. Express **12**(9), 1879 (2004).
[6] Terahertz database: http://www.thzdb.org, record TBM000001001
[7] J. Schöldström, U. Zimmermann, and M. Edoff, J. Phys. D: Appl. Phys. **45**, 115101 (2012).
[8] W. Witte, R. Kniese, and M. Powalla, Thin Solid Films **517**, 867 (2008).
[9] J. Olejnicek, C.A. Kamler, A. Mirasano, A.L. Martinez-Skinner, M.A. Ingersoll, C.L. Exstrom, S.A. Darveau, J.L. Huguenin-Love, M. Diaz, N.J. Ianno, and R.J. Soukup, Solar Energy Mater. Solar Cells **94**, 8 (2010).
[10] Y.H. Choi, Thin Solid Films **519**, 4390 (2011).
[11] V. Izquierdo-Roca, A. Pérez-Rodriguez, A. Romano-Rodriguez, J.R. Morante, J. Alvarez-Garcia, L. Calvo-Barrio, V. Bermudez, P.P. Grand, O. Ramdani, L. Parissi, and O. Kerrec, J. Appl. Phys. **101**, 103517 (2007).
[12] J. Álvarez-García, B. Barcones, A. Pérez-Rodríguez, A. Romano-Rodríguez, J.R. Morante, A. Janotti, S.-H. Wei, and R. Scheer, Phys. Rev. B **71**, 054303 (2005).
[13] F. Castellano, A. Bismuto, M.I. Amanti, R. Terazzi, M. Beck, S. Blaser, A. Bächle, and J. Faist, J. Appl. Phys. **109,** 102407 (2011).
[14] B.G. Lee, M.A. Belkin, C. Pflügl, L. Diehl, H.A. Zhang, R.M. Audet, J. MacArthur, D.P. Bour, S.W. Corzine, G.E. Hofler, and F. Capasso, IEEE J. Quantum Electron. **45**(5), 554 (2009).

Cu(In, Ga)Se$_2$ SLUOKSNIŲ INFRARAUDONOJI SPEKTROSKOPIJA IR VAIZDINIMAS

L. Minkevičius [a], S. Balakauskas [a], M. Šoliūnas [a], R. Suzanovičienė [a], J. Uždas [a], G. Molis [b], R. Juškėnas [a], A. Selskis [a], G. Niaura [a], G. Valušis [b,c], V. Tamošiūnas [a,c]

[a] *Fizinių ir technologijos mokslų centras, Vilnius, Lietuva*
[b] *TeraVil Ltd, Vilnius, Lietuva*
[c] *Vilniaus universiteto Fizikos fakultetas, Vilnius, Lietuva*

Santrauka

Pasaulyje sparčiai besivystant fotoelektros sektoriui bei tobulėjant plonasluoksnių saulės elementų technologijoms, vario indžio galio selenido (CIGS) pagrindu suformuoti lankstūs saulės elementai tampa vis patrauklesni masinei gamybai, o rekordinis tokių saulės elementų efektyvumas viršija 20 %.

Pristatomo darbo tikslas yra ištirti CIGS sluoksnių savybes infraraudonajame ir teraherciniame dažnių diapazonuose siekiant ateityje pritaikyti kompaktiškas vaizdinimo sistemas CIGS galutinės produkcijos parametrų (pvz., storio, kristalitų formavimosi rezultatų, kontaktų kokybės) kontrolei.

Bandiniai buvo užauginti magnetroninio dulkinimo įrenginiu iš vieno keturnario CIGS taikinio. Keičiant auginimo laiką, atstumą iki taikinio, po to atkaitinimo temperatūrą, užauginti skirtingų parametrų sluoksniai. Rentgeno spindulių difrakcijos metodu nustatyta struktūra. Kristalinei struktūrai patvirtinti atlikti Ramano spektroskopijos matavimai, išmatuoti infraraudonieji atspindžio spektrai. Analizuojant gautus duomenis nustatyta, kad šie spektrai gali būti panaudoti bekontaktiniam plonų sluoksnių storio ir kokybės įvertinimui. Skenuojančiu elektroniniu mikroskopu (SEM) atliktos nuotraukos iliustruoja paviršiaus morfologiją. Fourier spektrinius matavimus papildė tyrimai terahercų dažnių (THz) srityje. Gauti rezultatai taip pat atskleidžia galimybę stebėti apatinio molibdeno kontakto kokybę net su užaugintu ant viršaus CIGS sluoksniu.